Dalton Transactions

ROYAL SOCIETY OF CHEMISTRY

PAPER

View Article Online
View Journal | View Issue

Cite this: *Dalton Trans.*, 2025, **54**, 8586

Photo-Fenton degradation on Mo-doped $NiFe_2O_4$ photocatalyst†

Anshu Shrivastava, Uttam Kumar and Indrajit Sinha *

Received 3rd December 2024,
Accepted 28th April 2025

DOI: 10.1039/d4dt03359k

rsc.li/dalton

The poor photo-Fenton properties of $NiFe_2O_4$, a magnetic material, can be altered by appropriate metal ion doping. We carried out preliminary DFT and TD-DFT calculations and found that the photoexcited molybdenum doped $NiFe_2O_4$ interacts effectively with H_2O_2 for hydroxyl radical generation. Based on this prediction, we prepared Mo-doped $NiFe_2O_4$ and tested its photo-Fenton activity for tetracycline (TC) degradation. The Mo-doped $NiFe_2O_4$ nanoparticles were significantly finer in size and superparamagnetic, enabling easy after-use separation. Experimental and DFT calculation results showed that the Mo-dopant substitutes the Fe^{3+} occupying the octahedral site in $NiFe_2O_4$. Mo-doping extended the absorption edge and decreased the interfacial charge transfer resistance of $NiFe_2O_4$. The Mo-doped $NiFe_2O_4$ nanoparticles demonstrated excellent TC photo-Fenton degradation activity, along with appropriate recyclability. A combination of experimental and DFT calculation results indicated the possible photo-Fenton mechanism.

1. Introduction

The use of antibiotics in humans and animals has increased significantly over the past few decades due to climate change, pollution, and rapid economic development.[1] Tetracycline (TC), a commonly used antibiotic, has been extensively employed in human therapy, veterinary, and agricultural production.[2] Reports indicate that large amount of TC are annually discharged into the aquatic environment with wastewater.[3] Advanced oxidation processes (AOPs) utilizing highly reactive free radicals are effective and promising methods for mitigating environmental risks by degrading antibiotics like TC.[4] The conventional homogeneous Fenton process involves mixing a Fe^{2+} solution with H_2O_2 to produce $^{\bullet}OH$ ($Fe^{2+} + H_2O_2 \rightarrow Fe^{3+} + {}^{\bullet}OH + OH^-$).[5] The regeneration of Fe^{2+} from Fe^{3+} is a critical issue because the ($Fe^{3+} + H_2O_2 \rightarrow Fe^{2+} + {}^{\bullet}OOH + H^+$) back reaction is much slower than the forward reaction.[5] Issues like the requirement of a low (working) pH range (around 2 to 3) and high production of iron sludge residue due to limited Fe^{2+} regeneration seriously hinder the practical application of the homogeneous Fenton technique.[6]

In contrast, the photo-driven heterogeneous Fenton reaction, relying on efficient hydroxyl radicals ($^{\bullet}OH$) production from H_2O_2, is a green method favored for chemically degrading a wide range of non-biodegradable pollutants to their non-toxic fragments in the presence of iron-based photocatalysts.[7] Light of suitable wavelength photo-excites the semiconductor photocatalyst. The photo-excited electrons in the photocatalyst's conduction band (CB) reduce H_2O_2 to produce $^{\bullet}OH$ radicals, while oxidation occurs at the holes in the valence band (VB).[8] The separate oxidation and reduction sites in photo-Fenton photocatalysts enhance efficiency by overcoming the rate-limiting issues of conventional Fenton processes. Moreover, the process offers high catalytic efficiency, facilitated by the robust regeneration of Fe^{2+} by photoexcited electrons ($Fe^{2+} \rightleftharpoons Fe^{3+}$), ensuring continuous redox cycling. Additionally, it demonstrates broader pH tolerance, with simple operational requirements, mild reaction conditions, and overall higher efficiency.

The spinel $NiFe_2O_4$ semiconductor is a prospective candidate for the photo-Fenton degradation of organic pollutants due to its moderate visible light band gap (1.9–2.2 eV) and good photochemical stability.[9] Crucially, the superparamagnetic behavior of $NiFe_2O_4$ nanoparticles allows their easy separation from aqueous solutions and re-dispersal by simple application and removal of the applied magnetic field. Nonetheless, pristine $NiFe_2O_4$ characteristically exhibits low surface reaction rates, rapid recombination of photogenerated electrons and holes, and poor visible light absorption.[10] Various strategies have been employed to address these shortcomings and enhance its catalytic efficiency. A promising

Department of Chemistry, Indian Institute of Technology (Banaras Hindu University), Varanasi 221005, India. E-mail: isinha.apc@iitbhu.ac.in

†Electronic supplementary information (ESI) available: Instruments used for material characterizations, equations for structural parameters calculations, ionic radius table, particle size distribution graph, Tauc plots, photo-Fenton experiment results, TOF comparison table, potential energy DFT calculations, DFT calculated UV visible spectrum, interaction energy DFT calculations. See DOI: https://doi.org/10.1039/d4dt03359k

approach is metal ion doping to alter the physical and chemical properties of spinel $NiFe_2O_4$. Typically, the dopant level introduced in the band gap enhances charge separation and slows the recombination process. There are a few instances of the metal-doped $NiFe_2O_4$ photocatalysis. Thus, Alzahrani *et al.* reported the synthesis of Nd-doped $NiFe_2O_4$ and Gd-doped $NiFe_2O_4$ photocatalysts for photocatalytic degradation of organic effluents. They observed the superior photocatalytic activity of doped $NiFe_2O_4$ samples than bare $NiFe_2O_4$ due to reduction in the recombination of electrons and holes.[11,12] Similarly, enhancement in the photocatalytic activity of Co-doped $NiFe_2O_4$ and Mg-doped $NiFe_2O_4$ were ascribed to dopant energy states slowing the recombination of electrons and holes.[13,14]

In this regard, molybdenum (Mo) is a particularly suitable dopant, as it can modify the electronic properties (carrier concentration or CB position) and reduce the recombination of photogenerated charge carriers. Mo exists in multiple oxidation states (+4, +5, and +6), and the dopant energy level in the $NiFe_2O_4$ band gap can improve the iron cycle ($Fe^{2+} \rightleftharpoons Fe^{3+}$) in Fenton catalysis, enhancing catalytic efficiency. For instance, Ying *et al.* found that the TiO_2 doped by Mo^{6+} extends the absorption edge and decreases the interfacial charge transfer resistance. The photocatalytic activity of Mo-doped TiO_2 was much better than pure TiO_2.[15] Likewise, in a recent report, authors have shown that Mo-doped FeS_2 demonstrates improved stability and photo-Fenton activity.[16] Considering the advantages mentioned and the variable oxidation states of Mo, which are crucial for the Fenton reaction, this study explores the photo-Fenton activity of Mo-doped $NiFe_2O_4$. Notably, there has been no investigation into the design and effects of Mo-doping in spinel $NiFe_2O_4$ on its photo-Fenton TC degradation activity, making this investigation a novel contribution to the field.

Previous studies,[17–19] combining experimental and computational approaches, indicate that for a photo-Fenton catalyst to be effective, its photo-excited CB must interact favourably with H_2O_2, to facilitate $^{\bullet}OH$ radical production. Guided by this principle, in the present work, we employed density functional theory (DFT) and time-dependent DFT (TD-DFT) calculations to qualitatively evaluate whether the Mo doped $NiFe_2O_4$ satisfies this criterion, prior to experimental investigations. The following description highlights the novelty of this research work. There is no previous investigation on photocatalytic properties of Mo-doped $NiFe_2O_4$. The Mo-dopant can act as a donor dopant level and a shallow trap in the $NiFe_2O_4$ band gap preventing photoexcited electron–hole recombination, improving charge separation and extended carrier lifetimes. Moreover, favourable Mo^{6+}/Mo^{5+} redox potential also implies the possibility of increased Fe^{3+} to Fe^{2+} back reaction rate. Critically, we use DFT and TD-DFT calculations to predict that Mo doping results in charge redistribution, altered electronic transitions and facilitates efficient $^{\bullet}OH$ generation through enhanced H_2O_2 activation. Hence, such doping can substantially enhance the photocatalytic activity of Mo-doped $NiFe_2O_4$. The improved activity, along with the superparamagnetic properties of the doped $NiFe_2O_4$ nanoparticles (enabling easy recovery and redispersal of the nanoparticles for reuse), could result in an industrially attractive photocatalyst.

Satisfied by the DFT calculation results and the possibility of enhanced photocatalytic activity of this novel doped nanomaterial, we synthesized Mo-doped $NiFe_2O_4$ nanoparticles by a one-step hydrothermal protocol. Comprehensive materials characterizations were conducted to examine the physicochemical properties, microstructure, chemical composition, optical magnetic properties of the prepared Mo-doped $NiFe_2O_4$ catalysts. Mott–Schottky and electrochemical impedance spectroscopy (EIS) were used to calculate the flat band potential, semiconductor type, and charge transfer resistance. The effects of Mo-dopant amount, H_2O_2 concentration, and pH on TC degradation were systematically investigated. Under visible light irradiation, the synthesized Mo-doped $NiFe_2O_4$ nanoparticles demonstrated enhanced photo-Fenton degradation of tetracycline. Scavenger experiments identified the key reactive species responsible for the photocatalytic activity. Experimental and DFT calculation results were combined to understand the photocatalytic mechanism in this photo-Fenton process.

2. Experimental section

2.1. Materials used for experimental procedures

AR grade precursor materials $Ni(NO_3)_2{\cdot}6H_2O$ (Merck), $Fe(NO_3)_3{\cdot}9H_2O$ (Merck), $(NH_4)_6Mo_7O_{24}{\cdot}4H_2O$ (Merck), and NaOH (Merck) were used for experimental procedures without extra purification. Double distilled water (DW) was used as a solvent for all the experiments in this research.

2.2. Hydrothermal synthesis of Mo-doped $NiFe_2O_4$ nanoparticles

Pure and Mo doped $NiFe_2O_4$ samples with various atomic percentage (at%) of Mo doping were synthesized by hydrothermal method. Firstly, 0.0125 mmol of $(NH_4)_6Mo_7O_{24}{\cdot}4H_2O$ and 2.4875 mmol of $Fe(NO_3)_3{\cdot}9H_2O$ salts were mixed in 40 ml of distilled water with continuous stirring for one hour. Then 1.25 mmol of $Ni(NO_3)_2{\cdot}6H_2O$ was dissolved into the earlier prepared salt solution to give mixture with $[Ni^{2+}]/([Mo^{6+}] + [Fe^{3+}])$ molar ratio of 0.5. The aforesaid reaction mixture was then treated to a dropwise addition of 1 M NaOH until its pH reached 12. The reaction mixture was stirred for three more hours, until a brown precipitate formed. At this point, the mixture was placed in an autoclave and heated to 180 °C for 24 hours. After carefully washing the resulting dark brown precipitate with distilled water and ethanol, it was dried at 70 °C in an oven.

The above-mentioned synthesis procedure outlines the synthesis of 1% Mo doped $NiFe_2O_4$ nanoparticles. The 2% and 4% Mo-doped $NiFe_2O_4$ nanoparticles were synthesised in a similar manner, with the only difference being the amount of $(NH_4)_6Mo_7O_{24}{\cdot}4H_2O$ utilised in the synthesis. The synthesized

Mo-doped $NiFe_2O_4$ samples were abbreviated as 1MNFO, 2MNFO, and 4MNFO in accordance with the increasing at% corresponding to 1 at%, 2 at%, and 4 at% Mo-dopant in $NiFe_2O_4$, respectively. Pure $NiFe_2O_4$ was prepared by an analogues protocol but without the addition of $(NH_4)_6Mo_7O_{24}{\cdot}4H_2O$ salt.

2.3. Control experiments on catalytic/photocatalytic activity of the nanocomposites

The 1MNFO sample was first tested for Fenton activity toward tetracycline (TC) degradation in the dark. In another control experiment the 1MNFO sample was also tested for TC degradation activity in aqueous medium under visible light irradiation (but without H_2O_2). Little or negligible TC degradation was observed under these reaction conditions.

2.4. Photo-Fenton catalytic activity

The photo-Fenton activities of the synthesized catalysts (undoped $NiFe_2O_4$, 1MNFO, 2MNFO, and 4MNFO) were examined for TC degradation under cool white 14 W LED light (intensity: 1430 W m^{-2}) irradiation. Fig. S1† shows the emission spectrum of this LED light. A 1 mg ml^{-1} dispersion of photocatalyst nanoparticles was prepared by introducing the required amount of nanoparticles in the specified volume of double distilled water and bath sonicating for 20 minutes. In each experiment, 3 ml of 10 ppm TC aqueous solution with 100 μL of earlier prepared photocatalyst suspension was taken in a 3.5 ml quartz cuvette having 1 cm pathlength. The resulting mixture was kept in the dark for 30 minutes until the establishment of the adsorption–desorption equilibrium. An adequate amount of H_2O_2 was then added to the mixture. This reaction mixture was then exposed to visible light. The absorption spectrum of the TC solution was recorded at regular intervals after separating the photocatalyst with a magnet. The absorbance was measured at 358 nm, the characteristic absorption peak of TC. As TC degradation progresses, the intensity of the characteristic absorption peak diminishes. The experimental details have been discussed in the section S1 of ESI.†

Several control experiments were carried out under various conditions. For instance, experiments were conducted at different pH values to determine the optimal reaction pH. The effect of H_2O_2 dosage on the photo-Fenton activity was also investigated by evaluating the photo-Fenton activity of Mo-doped $NiFe_2O_4$ sample at various H_2O_2 concentrations in the reaction mixture. Finally, the best photocatalyst with the highest photo-Fenton activity among the Mo-doped $NiFe_2O_4$ samples was assessed under optimal pH and H_2O_2 conditions.

Separate scavenger experiments were carried out to investigate $OH^{\bullet}$ radical, photogenerated electrons/holes, and superoxide anion radical generation in the photo-Fenton degradation process. Isopropyl alcohol (IPA), $AgNO_3$, and triethanolamine (TEOA) were used to capture $OH^{\bullet}$, electrons, and holes, respectively. For the active species determination experiment, 100 μL of 0.185 mM IPA or 20 μL of 0.5 M TEOA, or 10 μL of 0.82 mM $AgNO_3$ were added to the reaction mixture. The rest of the experiment remained the same. On the other hand, the nitro blue tetrazolium (NBT) test detected the superoxide radical anion formation ($O_2^{\bullet-}$). All the photo Fenton degradation experiments were conducted at ~27 °C temperature. The degradation efficiency (%) of each photocatalyst was calculated by eqn (1),

$$\text{Degradation efficiency } (\%) = \frac{(C_0 - C_e) \times 100}{C_0} \quad (1)$$

In eqn (1), C_0 and C_e represent the initial and equilibrium concentrations of TC in the reaction mixture (mg L^{-1}).

2.5. DFT calculations

The location of Mo dopant in the $NiFe_2O_4$ lattice was determined by plane-wave DFT calculations. These calculations were performed using the MedeA VASP (Vienna *ab initio* simulation package) software (Version 5.4.4). The calculations used generalized gradient approximation Perdew–Burke–Ernzerhoff (GGA-PBE) exchange–correlation functional[20] and the projected wave (PAW) pseudopotentials. The (56 atom) unit cell of the FCC inverse spinel $NiFe_2O_4$ (MP-22684)[21] was optimized using 2 × 2 × 2 *k*-points and 550 eV energy cut-off. Magnetic effects of $NiFe_2O_4$ were taken into consideration by using the spin-polarized calculations. The optimized unit cell is labelled as N0 in the rest of the manuscript (Fig. S2a and S2b†). The four different Mo-substituted $NiFe_2O_4$ models were built in which the dopant substitutes different sites (Fig. S3(a–d)†). The models have the dopant Mo atom substituting (1) the octahedral Fe (denoted by N1), (2) the tetrahedral Fe (denoted by N2), (3) the octahedral Ni (denoted by N3), and (4) occupying an interstitial position (denoted by N4) in the optimized $NiFe_2O_4$ lattice (N0 model). These four models were optimized with the same calculation parameters as mentioned above. The convergence criteria for structure optimization were set to (1) energy tolerance of 1.0×10^{-5} eV, (2) maximum force tolerance of 0.02 eV. The formation energies of the four doped systems were calculated using the following eqn (2)–(5).

$$E_f = E_{defect}(N1) - (E_{perfect}(NiFe_2O_4) - \mu_{Fe} + \mu_{Mo}) \quad (2)$$

$$E_f = E_{defect}(N2) - (E_{perfect}(NiFe_2O_4) - \mu_{Fe} + \mu_{Mo}) \quad (3)$$

$$E_f = E_{defect}(N3) - (E_{perfect}(NiFe_2O_4) - \mu_{Ni} + \mu_{Mo}) \quad (4)$$

$$E_f = E_{defect}(N4) - (E_{perfect}(NiFe_2O_4) + \mu_{Mo}) \quad (5)$$

In eqn (2)–(5) E_f is the defect formation energy, $E_{perfect}$ represents the energy of N0 model, E_{defect} depicts the energy of the Mo doped optimized model; μ_{Ni}, μ_{Fe}, and μ_{Mo} are the chemical potentials of Ni, Fe, and Mo atom *i.e.* the energy per atom. The unit cell of Ni (COD #9012985), Fe (COD #9015972), Mo (COD #9008474) was taken from Crystallography Open Database (COD). The geometry of the optimized model having most negative defect formation energy gives the location of Mo dopant in $NiFe_2O_4$ lattice.

The optimized Mo-doped $NiFe_2O_4$ model with the most negative formation energy was subjected to further processing.

A cluster of Mo-doped $NiFe_2O_4$ was cleaved from a suitable supercell of this model using the MAPS 4.4.1 software (released by Scienomics).[22] The unsaturated terminal oxygens of this cluster were passivated by hydrogens in the GaussView 6.0 software. In this cluster (having total 33 atoms), Ni occupies an octahedral site (abbreviated as Ni(Oct)), Mo occupies another octahedral site (denoted as Mo(Oct)), one Fe occupies an octahedral site (abbreviated as Fe(Oct)) and another Fe is in a tetrahedral site (denoted by Fe(Td)). Since, the cluster has been carved out of an optimized supercell, therefore, a single point DFT calculation was performed on this cluster using the DGDZVP basis set with the B3LYP (Becke-3-parameter-Lee–Yang–Parr) functional in the Gaussian 16 software.[23] This Mo-doped $NiFe_2O_4$ cluster model is denoted by the abbreviation 'MoNIF' cluster throughout this research work.

In the next step, the H_2O_2 molecule was built by GaussView 6.0 software. This molecule was optimized by Gaussian 16 software at the same level of theory as earlier. Fig. S4† shows the optimized structure of H_2O_2 molecule. DFT calculations were conducted to investigate the interaction of H_2O_2 with the MoNIF cluster in the ground state. All DFT calculations were performed at the same level of theory as discussed earlier. Natural bond orbital (NBO) analysis gave the charge transfer/delocalization due to the H_2O_2-MoNIF interaction. All calculations were performed in the gas phase.

2.6. TD-DFT calculations

Excited state TDDFT calculations at the same level of theory as the ground state calculations gave the gas phase UV-visible spectrum of the MoNIF cluster. The HOMO and LUMO locations in the cluster corresponding to the most intense excitation frequency were calculated. Separate TDDFT calculations (gas phase) were carried out to investigate the interaction of H_2O_2 with the excited state HOMO location of the MoNIF cluster.

3. Results and discussion

3.1. Material characterization

The samples prepared for this study were characterized through X-ray diffraction (XRD), scanning electron microscopy (SEM), X-ray photoelectron spectroscopy (XPS), vibrating sample magnetometer (VSM), high-resolution transmission electron microscopy (HRTEM), ultraviolet-visible (UV–Vis) spectrophotometer, and ultraviolet visible diffuse reflectance spectrophotometer (UV-DRS) *etc*. The experimental features for these characterization techniques are provided in the section S2 of the ESI.†

Fig. 1a and b present the powder XRD patterns of pure $NiFe_2O_4$ alongside the Mo-doped samples, *i.e.*, 1MNFO, 2MNFO, and 4MNFO nanoparticles. The XRD pattern for pure $NiFe_2O_4$ exhibits distinct diffraction peaks at 18.4°, 30.2°, 35.7°, 37.3°, 43.3°, 53.8°, 57.2°, 62.9°, and 74.4° (2θ) values. These correspond to the (111), (220), (311), (222), (400), (422), (511), (440), and (533) crystal planes of the inverse spinel $NiFe_2O_4$ structure (JCPDS file 74-2081).[24] Similarly, the XRD patterns of 1MNFO, 2MNFO, and 4MNFO match those of $NiFe_2O_4$ (JCPDS file 74-2081). No additional peaks were detected, confirming the incorporation of Mo into the $NiFe_2O_4$ lattice.

Notably, the XRD patterns of Mo-doped samples exhibit a slight shift to lower 2θ values, indicating an increase in *d*-spacing (interplanar distance) as the Mo content rises (Fig. 1b). Table 1 gives the magnitude of lattice expansion (details of lattice parameter calculation given in ESI†). The expansion is due to the dopant's lattice position in the $NiFe_2O_4$ inverse spinel structure. To understand this, we compare the ionic radii of the metal ions in $NiFe_2O_4$, along with Mo in its +5 and +6 oxidation states in Table S1.†[25] The XPS results later show that the dopant Mo in the doped $NiFe_2O_4$ samples exist in +5 and +6 oxidation states. For this reason, Table S1† also displays the ionic radii of Mo in its +5 and +6 oxidation states. Mo doping into the $NiFe_2O_4$ structure

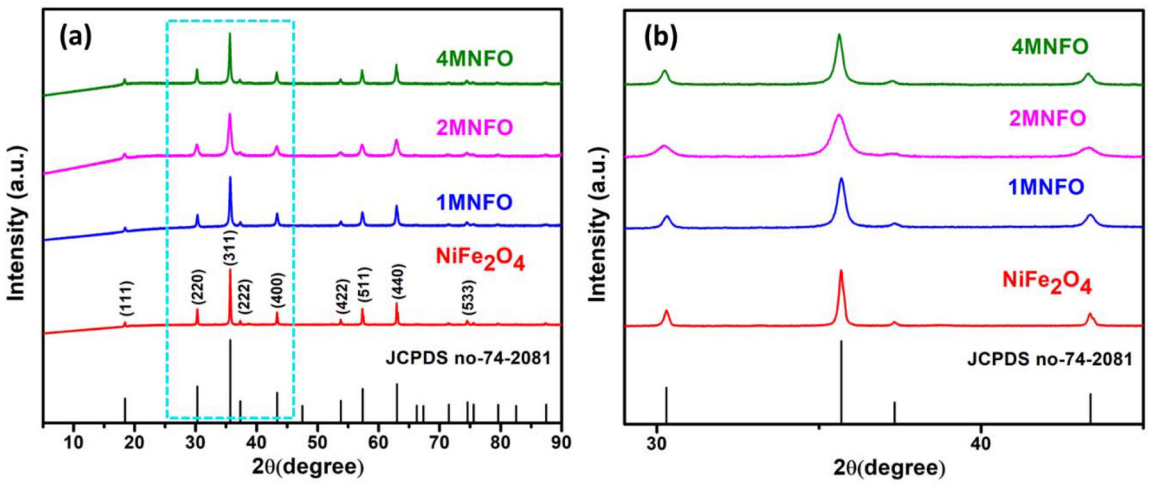

Fig. 1 (a and b) XRD of pure $NiFe_2O_4$, 1MNFO, 2MNFO, and 4MNFO samples.

Table 1 Structural parameters for $NiFe_2O_4$, 1MNFO, 2MNFO, and 4MNFO nanoparticles

Nanoparticle	Crystallite size (nm)	Lattice parameter (Å)
Pure $NiFe_2O_4$	42.87	8.343
1MNFO	27.02	8.344
2MNFO	17.34	8.347
4MNFO	28.05	8.358

Section S3† provides the equation's details used for calculation of structural parameters.

could occur in two ways: if Mo substitutes a larger cation, such as Ni^{2+}, in the octahedral position, lattice contraction would be expected. Conversely, lattice expansion should occur if Mo replaces a smaller cation like Fe^{3+} in an octahedral position. Thus, lattice expansion implies Mo could be substituting Fe^{3+} in the octahedral sites of the $NiFe_2O_4$ lattice.

Column 2 of Table 1 shows the crystallite sizes of both doped and un-doped $NiFe_2O_4$ samples. The crystallite size decreases from 42.87 nm to 17.34 nm as the Mo-dopant increases to 2% (2MNFO). However, Mo doping beyond 2% increases the crystallite size. This is possibly due to the dopant limiting crystallite growth by slowing the nucleation rate during crystallization (Table 1).[26]

The morphology and microstructure of pristine $NiFe_2O_4$ and the 1MNFO samples were examined using TEM and SEM techniques. TEM images (Fig. 2a) reveal that pure $NiFe_2O_4$ particles exhibit a combination of octahedral (Oct) and nanosheet (NS) like morphologies. The high-resolution TEM (HR-TEM) analysis (Fig. 2b) shows a lattice *d*-spacing of 0.294 nm, corresponding to the (220) crystal plane of FCC $NiFe_2O_4$. This observation conforms to the XRD results, further confirming the crystalline structure of $NiFe_2O_4$ (JCPDS no.-74-2081). The *d*-spacing between adjacent lattice planes was measured using Digital Micrograph (Gatan) software. Similarly, Fig. 2c illustrates the morphology of 1MNFO particles, which retain an approximately octahedral shape even after Mo-doping. The HR-TEM image of 1MNFO (Fig. 2d) shows lattice fringes with a *d*-spacing of 0.309 nm, consistent with the (220) crystal plane. This slight increase in *d*-spacing from 0.294 nm to 0.309 nm aligns with the XRD results, confirming the successful incorporation of molybdenum into the $NiFe_2O_4$ nanoparticles. The particle size distribution of $NiFe_2O_4$ and 1MNFO samples have been calculated and given in the Fig. S5 of ESI.† Mo doping of $NiFe_2O_4$ decreases the average particle size from 75–95 nm ($NiFe_2O_4$) to 25–45 nm (1MNFO). The polydispersity index (PDI) was determined using eqn (S3) and (S4), provided in the section S4 of ESI.† Before Mo doping, pristine $NiFe_2O_4$ exhibi-

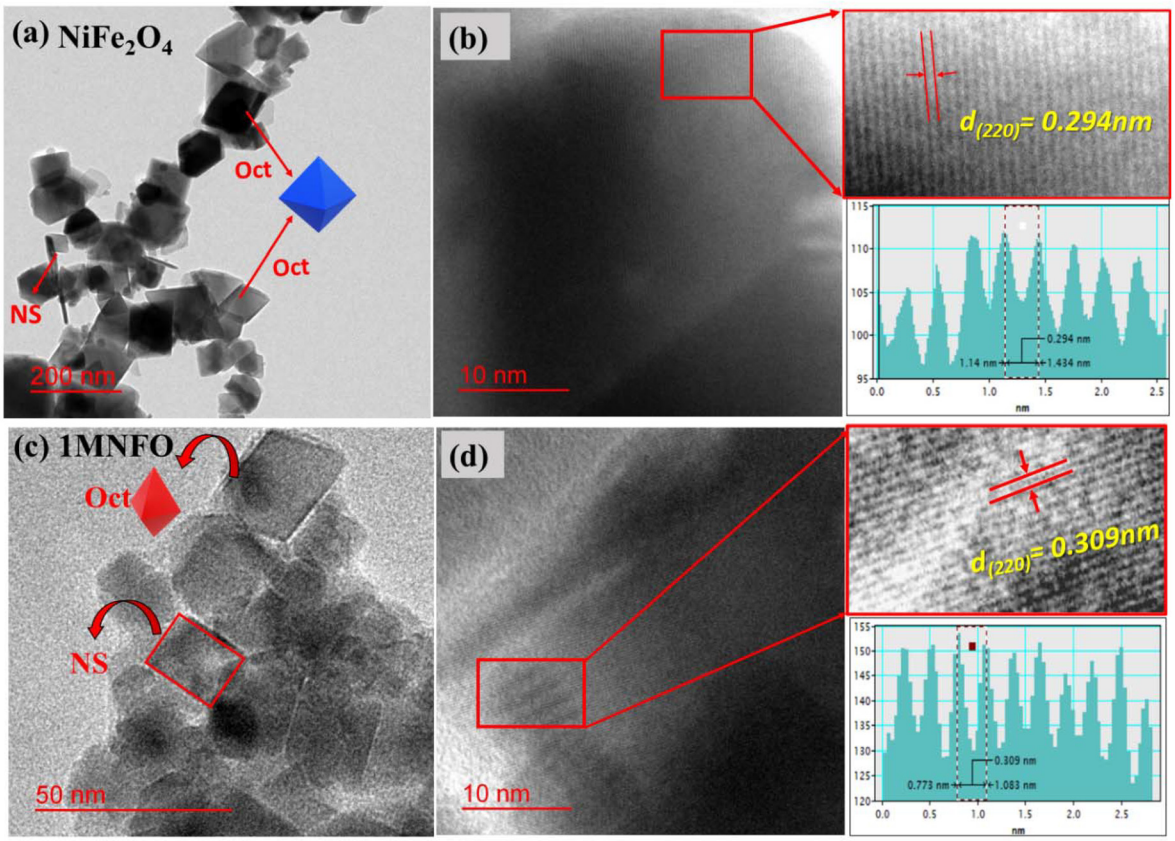

Fig. 2 (a) TEM and (b) HR-TEM and inverse fast Fourier transform (IFFT) images of $NiFe_2O_4$, (c) TEM and (d) HR-TEM and IFFT images of 1MNFO sample (note – 'NS' denotes nanosheet, 'Oct' denotes octahedron).

ted a PDI of 0.099, indicating a monodisperse nanoparticle distribution. In contrast, the 1MNFO sample displayed a PDI of 0.126, suggesting a transition to a moderately polydisperse nanoparticle system.

Fig. 3a and b show a SEM micrograph of the as-synthesized 1MNFO nanoparticles and its elemental mapping. The latter shows that the Mo-dopant is homogeneously distributed in the 1MNFO sample (Fig. 3b).

The VSM analysis gives the magnetic characteristics of the photocatalyst. Fig. 4 shows the VSM analysis for pure $NiFe_2O_4$ and 1MNFO by hysteresis loop plotted between magnetization (emu g^{-1}) *versus* applied magnetic field (O_e). The saturation magnetization for pure $NiFe_2O_4$ is 39.70 emu g^{-1}. After Mo doping, the saturation magnetization of 1MNFO was reduced to 20.30 emu g^{-1}. The absence of a hysteresis loop indicates that the pure and doped sample is superparamagnetic. The magnetization of both samples is sufficient for their separation from water by a magnet.

The XPS of pure $NiFe_2O_4$ and 1MNFO samples were carried out to determine the chemical composition of the photocatalyst surface and the oxidation states of the elements present. Fig. 5a displays the Ni 2p spectrum of $NiFe_2O_4$ and 1MNFO samples. The $NiFe_2O_4$ spectrum has Ni $2p_{3/2}$, and Ni $2p_{1/2}$ spin orbit doublets at 854.97 eV and 872.58 eV binding energies (B.E.) with two shake-up satellite peaks (denoted as 'sat.' in Fig. 5a), indicating Ni^{2+} occupies octahedral sites.[19] The fitted Ni 2p core-level spectrum of 1MNFO (Fig. 5a) also exhibits two shake-up satellites and spin–orbit doublets (Ni $2p_{3/2}$, Ni $2p_{1/2}$). The Ni $2p_{3/2}$ and Ni $2p_{1/2}$ spin–orbit doublets

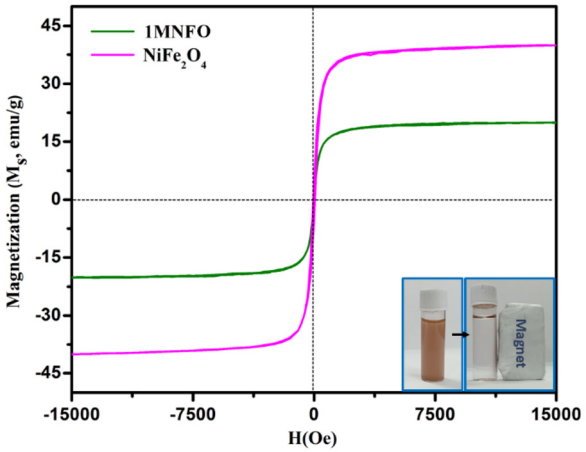

Fig. 4 Magnetization *versus* applied field plots of pure $NiFe_2O_4$, and 1MNFO nanoparticles.

at 855.39 and 873.02 eV show that Ni^{2+} occupies octahedral sites in the 1MNFO crystal structure.[19]

Fig. 5b compares the Fe 2p regions of bare $NiFe_2O_4$ and 1MNFO samples. The Fe 2p spectrum has two spin–orbit doublets (Fe $2p_{3/2}$, Fe $2p_{1/2}$) and two satellite peaks (denoted as 'Sat.' in Fig. 5b). Further deconvolution gave peaks at 709.98, 712.14, and 723.65, 726.28 eV, with two satellite peaks at 718.46 and 732.66 eV. These show that Fe^{3+} occupies octahedral and tetrahedral sites of the $NiFe_2O_4$ lattice.[27–30] The Fe 2p spectrum of 1MNFO also displays the Fe $2p_{3/2}$ and Fe $2p_{1/2}$

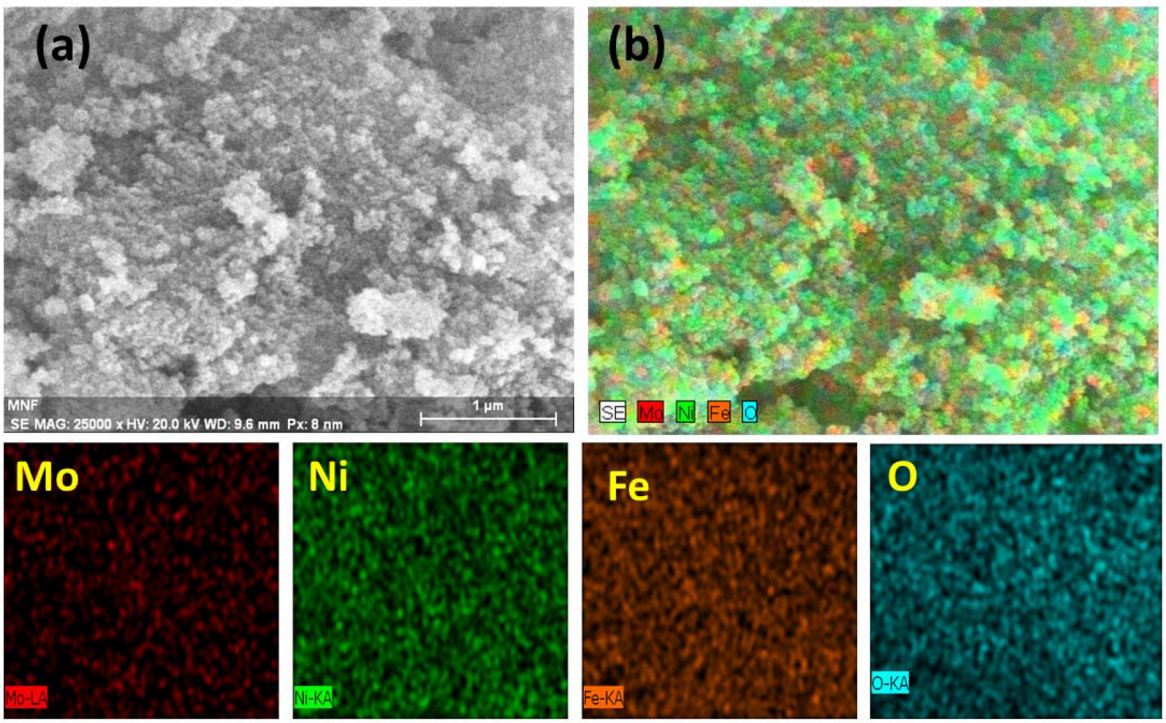

Fig. 3 (a) SEM images, and (b) elemental mapping of 1MNFO sample.

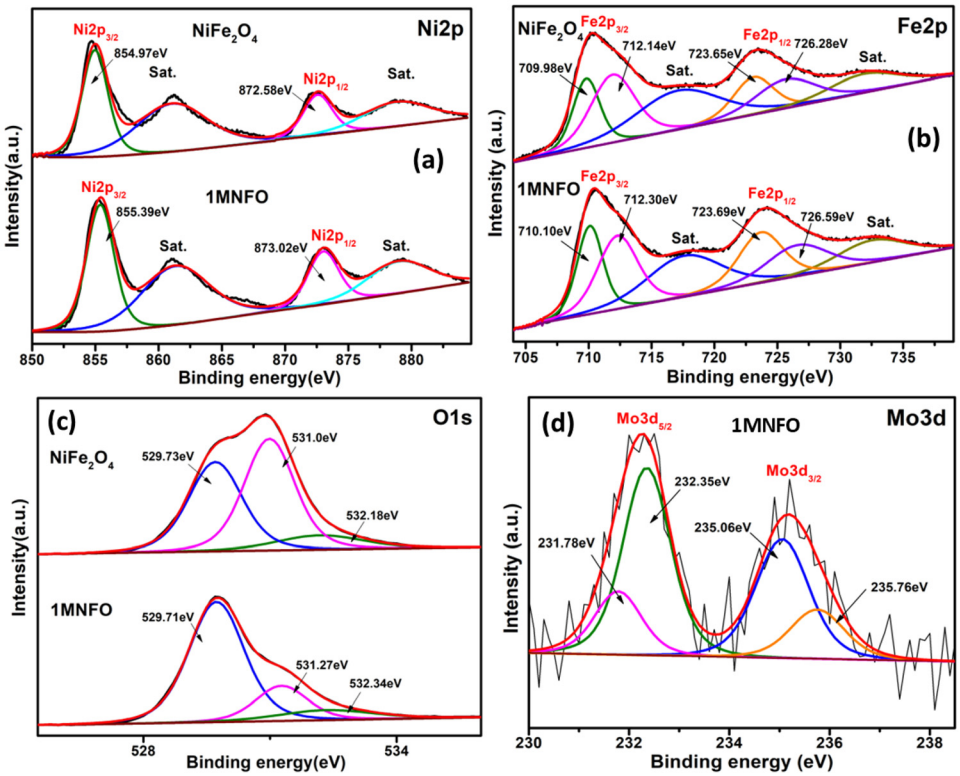

Fig. 5 High resolution comparative XPS spectra of, (a) Ni 2p, (b) Fe 2p, (c) O 1s, and (d) Mo 3d in pure $NiFe_2O_4$ and 1MNFO.

spin–orbit doublets. The Fe $2p_{3/2}$ part is deconvoluted into 710.10 and 712.30 eV, while the Fe $2p_{1/2}$ part fits peaks at 723.69 and 726.59 eV. These peaks, in combination with two satellite peaks at 718.59 and 732.51 eV binding energies, show that Fe^{3+} occupies octahedral and tetrahedral sites of the 1MNFO sample.[27,30] A comparison of the spectrum of $NiFe_2O_4$ and 1MNFO reveals that Mo-doping shifts the deconvoluted Fe2p peaks to slightly higher binding energies.

Fig. 5c presents the O 1s spectra of pure $NiFe_2O_4$ and 1MNFO samples. For pure $NiFe_2O_4$, three distinct deconvoluted peaks are observed at binding energies of 529.73, 531.0, and 532.18 eV, corresponding to metal–oxygen bonds (Ni–O or Fe–O),[31,32] oxygen vacancies,[33,34] and chemisorbed oxygen in –OH groups,[34,35] respectively (Fig. 5c). Upon Mo doping, the lattice oxygen deconvoluted O 1s peak shifts to a slightly lower 529.71 eV binding energy.[31,32] The other two O 1s peaks shift to slightly higher 531.27 and 532.34 eV binding energies. These are also attributed to oxygen vacancies[33,34] and chemisorbed oxygen[34,35] species, respectively (Fig. 5c). However, the area of oxygen vacancy peak and chemisorbed oxygen peak of pure $NiFe_2O_4$ decreased after Mo doping. This indicates that Mo dopants utilized chemisorbed oxygen to compensate for the oxygen vacancy and maintain charge balance in the lattice.

Fig. 5d displays the Mo 3d fitted spectrum region. Two major peaks are observed at 232.25 (Mo $3d_{5/2}$) and 235.18 eV (Mo $3d_{3/2}$) binding energies. Each of these peaks could be deconvoluted into two more peaks. The peaks at 231.78 and 235.06 eV indicate the presence of Mo in the +5 oxidation state, while the peaks at 232.35 and 235.76 eV correspond to Mo in the +6 state.[36–39] The higher valent Mo (in +6 oxidation state) dopant substitutes a Fe site in the $NiFe_2O_4$ lattice, causing oxygen deficiency. Oxygen vacancies are electron-rich, enabling the reduction of the higher-valent Mo^{6+} ions to Mo^{5+} ions.[38–40] Since higher-valent dopants require additional oxygen to maintain charge balance within the lattice, they tend to utilize chemisorbed oxygen to compensate for the oxygen deficiency. Consequently, this process leads to a reduction in the overall percentage of oxygen vacancies in the lattice.

Overall, Mo doping causes a slight shift in the Ni 2p and Fe 2p peaks towards higher binding energies. Concurrently, the lattice oxygen peak shifts to lower binding energy. These observations suggest that Mo doping facilitates charge transfer from the Ni and Fe sites to the lattice oxygen.

Fig. S6(a–d)† shows the band gap determination of pure $NiFe_2O_4$ and different Mo-doped $NiFe_2O_4$ samples, calculated by the Tauc equation. The graph was plotted between $(\alpha h\nu)^{1/n}$ *versus* photon energy ($h\nu$) to determine the band gap (where n = 1/2 for direct band). The symbols 'α', 'h', and 'ν' are referred to as absorption coefficient, Planck's constant, and photon's frequency in the Tauc relation. For direct transition, n equals 1/2, and 2 for indirect transitions.[41] The band gap (E_g) decreases from 2.014 ($NiFe_2O_4$) to 1.939 eV (2MNFO) after Mo-doping. The band gap of Mo-doped $NiFe_2O_4$ initially decreases and then increases with increasing Mo doping percentage after 2MNFO.

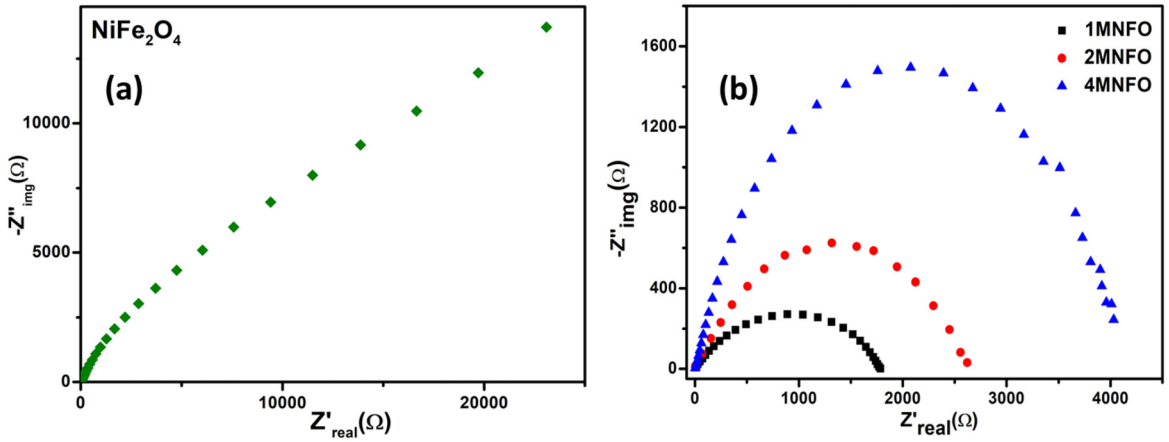

Fig. 6 Nyquist plot of (a) pure $NiFe_2O_4$ and (b) Mo-doped $NiFe_2O_4$ samples.

Electrochemical impedance spectroscopy (EIS) observations are related to the kinetics of charge carriers' recombination. Fig. 6a and b show the Nyquist plot of pure $NiFe_2O_4$, 1MNFO, 2MNFO, and 4MNFO samples. The diameter of semicircle of the Nyquist plot is directly proportional to the charge transfer resistance and inversely proportional to charge separation.[42] Among all samples, the Nyquist plot of 1MNFO had least semicircle diameter, indicating best charge separation during reaction.

Mott Schottky (MS) data were acquired at 500 Hz to ascertain the semiconductor type and calculate the band edge positions of $NiFe_2O_4$ and 1MNFO semiconductors. The equation $V(\text{NHE}) = V(\text{Ag/AgCl}) + 0.059\ \text{pH} + 0.197$ was used to convert the potential (V) to the normal hydrogen electrode (NHE) scale for the MS plots.[43] The pH of the electrolyte was approximately 6.8. Fig. 7a and b illustrate the MS plot of the pure $NiFe_2O_4$ and 1MNFO particles. Their MS plots show a positive slope, so pure $NiFe_2O_4$ and 1MNFO are n-type semiconductors. The pure $NiFe_2O_4$ and 1MNFO have CB edge potentials of −0.71 and −0.43 V, respectively. Equation $E_g = E_{VB} - E_{CB}$ was utilized to determine the VB edges of pure $NiFe_2O_4$ and 1MNFO using these CB edge values. The calculated VB edge is 1.31 V for pure $NiFe_2O_4$ and 1.535 V for the 1MNFO sample.

3.2. Photo-Fenton activity

Fig. S7a† shows that the dark Fenton TC degradation on 1MNFO at pH ~3 was approximately ~18% in 90-minute reaction time. Additionally, another control experiment was conducted under visible light irradiation using the 1MNFO sample without the external addition of H_2O_2. In this case, only ~8% TC degradation was observed (Fig. S7b†).

The photo-Fenton activities of Mo-doped and undoped $NiFe_2O_4$ for TC degradation have been investigated. Photo Fenton activities of the 1MNFO doped sample were studied at pH ~1, 3 and 6 (near neutral). Fig. S7c† shows that the best photo Fenton activity of 1MNFO was observed at pH 3. Another set of experiments were conducted to optimize H_2O_2 amount in the photocatalysis reaction mixture at pH 3

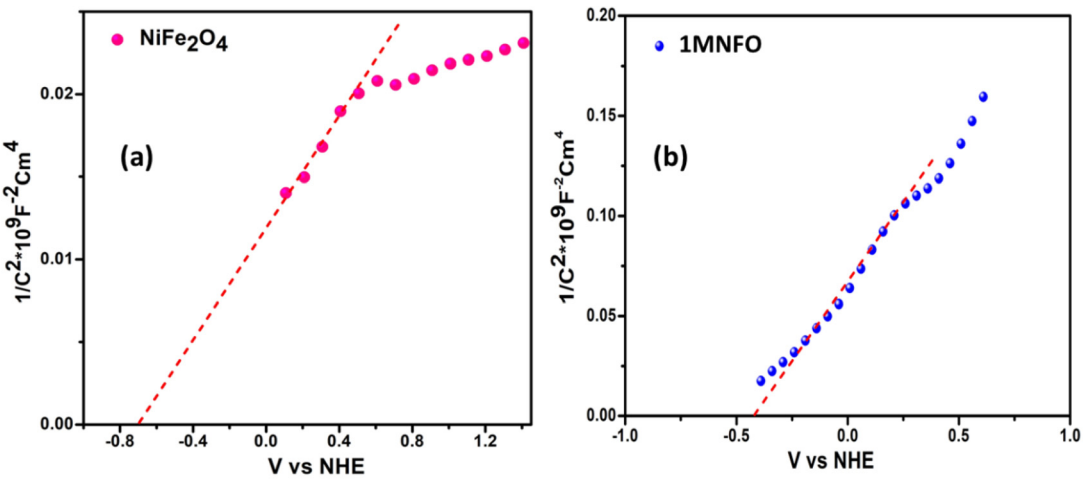

Fig. 7 Mott–Schottky plots for (a) pure $NiFe_2O_4$, and (b) 1MNFO photocatalyst.

(Fig. S7d†). The volume of H_2O_2 used in the experiments were 50 μl, 100 μl, and 150 μl of 0.5M H_2O_2. The best photo-Fenton activity on the 1MNFO sample was with 100 μl of H_2O_2 amount. Nearly, ~99% of photo-Fenton degradation of TC by 1MNFO was completed in 130 min (Fig. S7d†). Only 60% of TC degradation was observed when 150 μl of 0.5 M H_2O_2 was used. This reduction occurs because excess (unreacted) H_2O_2 acts as a hydroxyl radical ($^{\bullet}OH$) scavenger and generate hydroperoxyl radical ($^{\bullet}HO_2$) (shown in eqn (6) and (7)).[44] This $^{\bullet}HO_2$ radical is a considerably weaker oxidising agent than $^{\bullet}OH$ radical.[44]

$$H_2O_2 + {}^{\bullet}OH \rightarrow {}^{\bullet}HO_2 + H_2O \quad (6)$$

$$^{\bullet}OH + {}^{\bullet}HO_2 \rightarrow H_2O + O_2 \quad (7)$$

Fig. 8a displays the concentration *versus* time plots of TC degradation under optimum photo Fenton conditions on different Mo-doped and undoped $NiFe_2O_4$ samples. Among all photocatalysts, 1MNFO shows the best TC degradation photo-Fenton activity and undoped $NiFe_2O_4$ sample shows poor photo-Fenton activity. Fig. S7e† shows the UV-visible absorbance spectra of photo-Fenton degradation of TC by 1MNFO photocatalyst at pH 3. Within 130 min, ~99% of TC was degraded under visible light irradiation. Fig. 8b shows that the TC degradation concentration *versus* time data fits best pseudo-first-order kinetics ($0.988 < R^2 < 0.999$). Table S2† compares the photo-Fenton activity of our photocatalyst for tetracycline degradation with previous research work. The activity of the Mo-doped $NiFe_2O_4$ is among best reported in literature for doped semiconductors.

Separate active species trapping tests were conducted with IPA, $AgNO_3$, and TEOA. IPA is a hydroxyl radical scavenger, $AgNO_3$ is an electron scavenger, and TEOA serves as a hole scavanger.[45] The photo-Fenton reaction on the 1MNFO catalyst almost completely degraded tetracycline in 130 min without any scavenging agent. In comparison, the photo-Fenton TC degradation efficiencies on the 1MNFO sample with either IPA, or $AgNO_3$, or TEOA were ~15.9%, ~14.6%, and 95.5% (Fig. S7f†) respectively. This demonstrates that hydroxyl radicals and photogenerated electrons are the predominant active

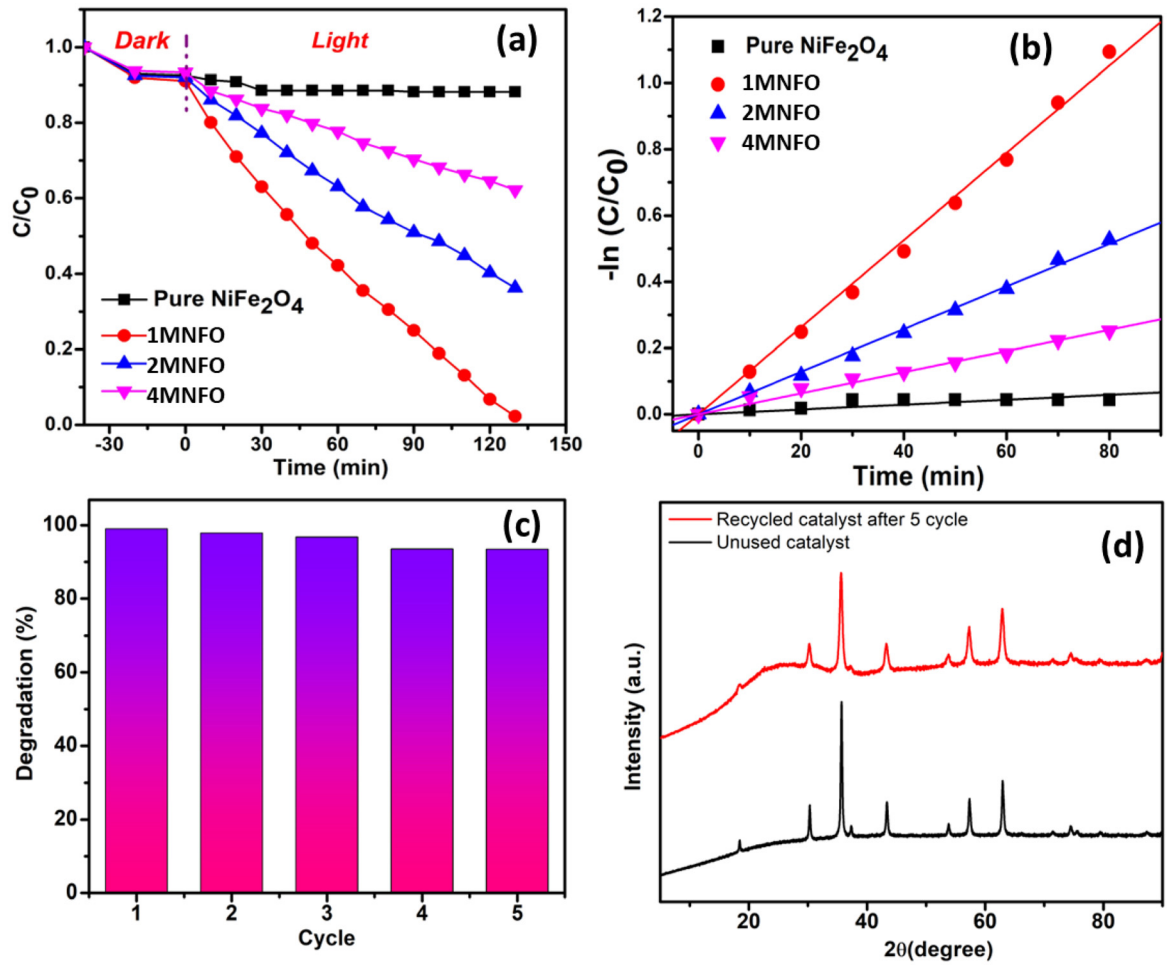

Fig. 8 (a) Comparison plot of photo-Fenton TC degradation activity of pure $NiFe_2O_4$, 1MNFO, 2MNFO, and 4MNFO. (b) Linear plot of pseudo-first order kinetics of pure $NiFe_2O_4$, 1MNFO, 2MNFO, and 4MNFO photocatalyst. (c) Recyclability test of 1MNFO composite, and (d) XRD patterns of unused and recycled catalyst (1MNFO) after 5 cycles.

species for photo Fenton TC degradation on the 1MNFO sample.

In addition to the above, the Nitro blue tetrazolium (NBT) test was used to detect the existence of superoxide radicals in the aqueous solution of 1MNFO photocatalyst.[46] Following the standard procedure, 3 ml of a 2.5×10^{-2} mM NBT solution was placed in a quartz cuvette, and 100 microliters of the dispersed photocatalyst nanoparticles (1 mg ml^{-1}) were added under (cool white LED) visible light irradiation. The supernatant was examined by UV-visible absorbance spectroscopy after the photocatalyst was separated using a magnet after fixed time intervals (Fig. S7g†). No change in the NBT molecule's absorption maximum at ~265 nm with time confirms that the superoxide radical ($^{\bullet}O^{2-}$) generation is negligible and is not an active species in TC degradation.

The recyclability test of 1MNFO was conducted for five consecutive cycles of photo-Fenton degradation of TC. The detailed experimental procedure is provided in section S5 of the ESI.† Fig. 8c illustrates the reusability of 1MNFO *via* consecutive experiments (5 cycles). The photo-Fenton activity of 1MNFO was ~91.5% after 5 cycles. Fig. 8d compares the XRD patterns of fresh and recycled 1MNFO samples. All XRD peaks of recycled 1MNFO match those of the unused fresh 1MNFO sample. The 1MNFO photocatalyst shows good photostability after five photocatalytic cycles.

The leaching concentration of Ni, Fe, and Mo metals of the recycled 1MNFO sample in the solution after the 5th photo Fenton degradation cycle was investigated using inductively coupled plasma-mass spectrometry (ICP-MS). The percentage concentrations of leached metal ions in the solution were Ni (0.98%), Fe (0.45%), and Mo (0.008%), respectively. The minor leaching of metal ions during the reuse of the 1MNFO sample results in a decrease in photo-Fenton activity of 1MNFO after five cycles.

XPS analysis was also done on the recycled 1MNFO sample (Fig. S8†). Fig. S8a† displays two spin–orbit doublet peaks at 854.26 (Ni $2p_{3/2}$) and 872.0 eV (Ni $2p_{1/2}$) binding energies, indicating Ni^{2+} in octahedral sites. Similarly, Fig. S8b† shows two spin–orbit doublet peaks (Fe $2p_{3/2}$ and Fe $2p_{1/2}$) and two satellite peaks in the fitted Fe 2p XPS spectrum. Further deconvolution confirmed the presence of Fe^{3+} in both octahedral and tetrahedral sites. Fig. S8c† represents the O 1s spectrum region. The three deconvoluted peaks obtained were similar to the fresh 1MNFO sample. These peaks indicate the presence of lattice oxygen (or metal–oxygen), oxygen vacancy, and chemisorbed oxygen species. A comparison of the XPS spectra of fresh and recycled 1MNFO samples (Fig. 5 and Fig. S8†) shows no significant change in Ni 2p, Fe 2p, and O 1s spectrum regions. Fig. S8d† shows deconvoluted Mo $3d_{5/2}$ peaks at 230.15 eV, 231.35 eV, and 232.50 eV due to Mo in the +4, +5, and +6 oxidation states. The Mo $3d_{3/2}$ peaks at 232.99 eV, 233.50 eV, and 234.70 eV are also due to Mo in the +4, +5, and +6 states in the recycled 1MNFO sample. Notably, the generation of Mo^{4+} after the fifth consecutive cycle of photo-Fenton TC degradation is likely due to the reduction of Mo^{6+}/Mo^{5+} by photogenerated electrons and oxygen vacancies.

3.3. DFT calculation results

DFT calculations give additional evidence supporting the experimental findings. The defect formation energies of N1, N2, N3, and N4 models were −0.32 eV, 0.52 eV, −0.08 eV, and 27.41 eV. Thus the model (N1), in which Mo substitutes Fe (Oct) atom, is most stable. Table S3† shows the expansion in $NiFe_2O_4$ lattice in all three dimensions after Mo doping. Notably, the XRD data analysis corroborates the DFT findings, confirming that Mo preferentially substitutes the Fe at the octahedral site. As detailed in section 2.5, all subsequent DFT and TD-DFT calculations were carried out on a Mo-doped $NiFe_2O_4$ cluster carved out of N1 called the 'MoNIF' model.

HOMO and LUMO locations give us the nucleophilic and electrophilic sites on the photocatalyst. In this context, ground state HOMO and LUMO positions indicate the nucleophilic and electrophilic sites before photoexcitation, while the excited state HOMO and LUMO positions on the photocatalyst give the nucleophilic and electrophilic positions after its photoexcitation. Fig. 9a displays the ground state HOMO LUMO locations on MoNIF cluster. The ground state HOMO is mainly on Ni(Oct) and Fe(Oct), while the LUMO is located partially on Fe(Oct), Fe(Td) and Mo(Oct) in the MoNIF cluster.

Next, single point TD-DFT calculation was carried out on the optimized MoNIF cluster. Fig. S9† displays the MoNIF cluster's simulated absorption spectra obtained from TD-DFT calculation. The vertical lines depict the excitations associated with electronic transitions at different wavelengths. The solid black curve in the figure displays the experimental solid-state UV-visible spectrum of the MoNIF cluster. The excited state HOMO–LUMO analysis was implemented on the oscillator frequency corresponding to the 552 nm (Fig. S9†) excited state. In the photo excited state, HOMO shifted from Ni(Oct), Fe(Oct) to Fe(Td) and lattice oxygens adjacent to the Mo metal centre (Fig. 9b).

After this DFT calculations were conducted to investigate the interaction of H_2O_2 with the Mo doped $NiFe_2O_4$ (MoNIF) cluster in the ground state and excited state. It was found that H_2O_2 interacts best with the octahedral Fe position when MoNIF is in its ground state. In contrast, H_2O_2 gives the lowest interaction energy with the tetrahedral Fe position (excited state HOMO location) when MoNIF is in the photoexcited state. The optimized H_2O_2 interaction structures are abbreviated as H_2O_2_Fe(Oct)_MoNIF_GS (H_2O_2 interacts with Fe (Oct) of MoNIF cluster in the ground state) and H_2O_2_Fe(Td) _MoNIF_ES (H_2O_2 interacts with Fe(Td) of MoNIF cluster in excited state) in the rest of the publication (Fig. 10a and b). Section S6 of ESI† displays the details of the H_2O_2 interaction potential energy calculations with MoNIF cluster in ground and excited states. Table S4† shows that the interaction energy for the H_2O_2_Fe(Td)_MoNIF_ES model has a negative value (−0.0053 Hartree) in contrast to positive value (0.0881 Hartree) found for the H_2O_2_Fe(Oct)_MoNIF_GS model.

Fig. 11(a–d) show the change in different bond lengths in H_2O_2_Fe(Oct)_MoNIF_GS, and H_2O_2_Fe(Td)_MoNIF_ES interaction systems. Fig. 11c shows that oxygen of H_2O_2 interacts

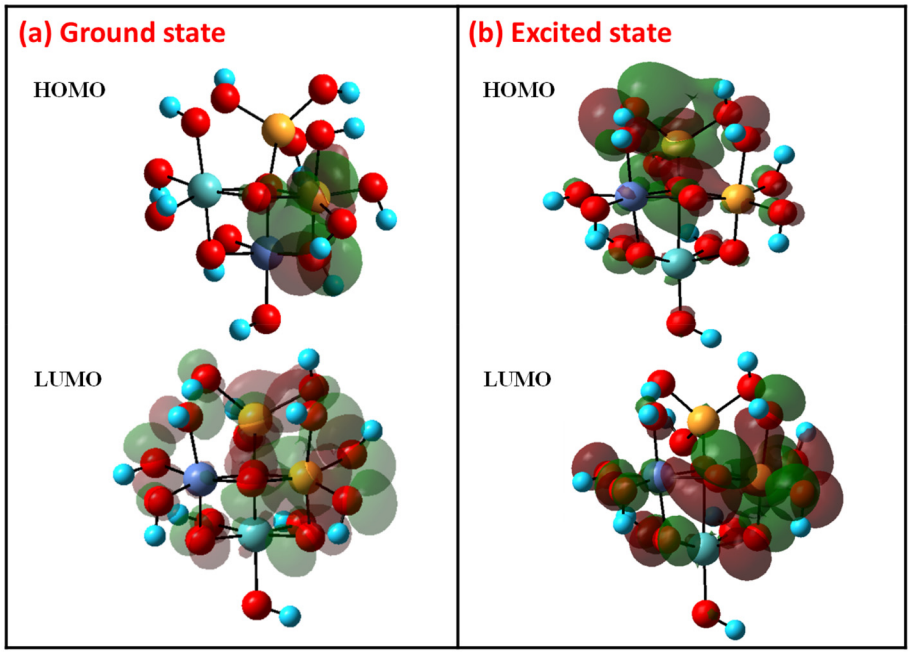

Fig. 9 The calculated HOMO/LUMO (a) ground state, and (b) excited state (552 nm) using DFT and TDDFT methods.

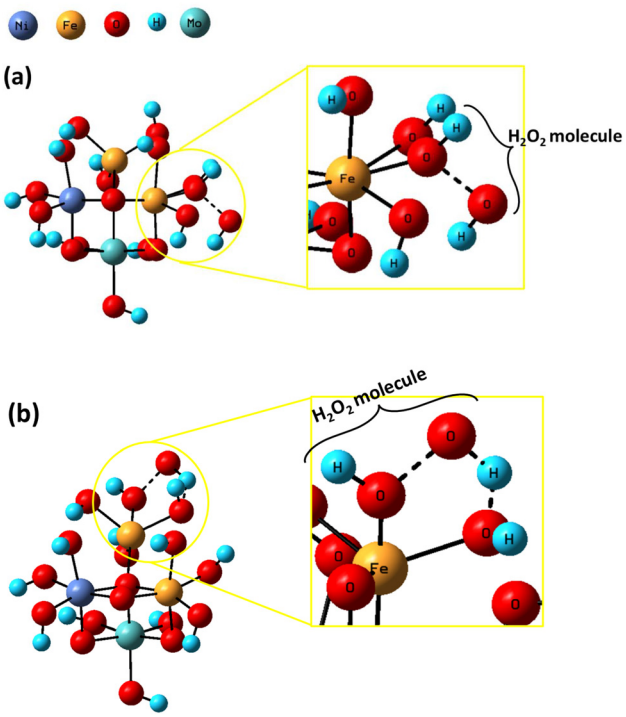

Fig. 10 The optimized structure of (a) H_2O_2_Fe(Oct)_MoNIF_GS, and (b) H_2O_2_Fe(Td)_MoNIF_ES systems.

with Fe(Oct) of MoNIF system in H_2O_2_Fe(Oct)_MoNIF_GS model. Fig. 11d shows that oxygen of H_2O_2 interacts with Fe (Td) and the terminal hydrogen of H_2O_2 interacts with oxygen coordinated to Fe(Td) in H_2O_2_Fe(Td)_MoNIF_ES system. The O_α–O_β bond length of H_2O_2 part in H_2O_2_Fe(Oct)_MoNIF_GS, and H_2O_2_Fe(Td)_MoNIF_ES systems is 1.686 Å, and 1.763 Å. The longer or more weakened O_α–O_β bond of H_2O_2, signifies greater bond activation. Thus, O_α–O_β bond activation is substantially more in the H_2O_2_Fe(Td)_MoNIF_ES interaction system, in line with the negative (or lower) interaction energy for this system.

Natural bond orbital (NBO) calculations at the same level of theory (Table 2) as earlier were performed on optimized H_2O_2_Fe(Oct)_MoNIF_GS, and H_2O_2_Fe(Td)_MoNIF_ES conformations to calculate the second-order stabilization energy $E^{(2)}$ due to electron delocalization. The abbreviations for atom types in Fig. 11c and d systems have also been used to describe the NBO analysis results. Eqn (8) employs second-order perturbation theory to calculate this energy $E^{(2)}$.[47]

$$E^{(2)} = q_i \frac{(F_{i,j})^2}{(\varepsilon_j - \varepsilon_i)}, \quad (8)$$

In eqn (8), q_i = donor orbital occupancy, ε_i = energy of accepter NBO, ε_j = energy of donar NBO, $F_{i,j}$ = off diagonal Fock matrix element. $E^{(2)}$ values quantify the delocalization adjustments to the corresponding zeroth-order natural Lewis structure.

Table 2 shows the significantly larger charge transfers (or delocalization) in the H_2O_2_Fe(Td)_MoNIF_ES system compared to the H_2O_2_Fe(Oct)_MoNIF_GS interaction system. The H_2O_2_Fe(Oct)_MoNIF_GS system, displays a weak charge transfer from LP(Fe_{Oct}) to BD*(O_α–O_β) with 0.52 kcal mol^{-1} interaction energy ($E^{(2)}$ value). Simultaneously, there is a reverse charge transfer from BD(O_α–O_β) to LP*(Fe_{Oct}) with 4.51 kcal mol^{-1} $E^{(2)}$ value. These weak charge transfers cause only a

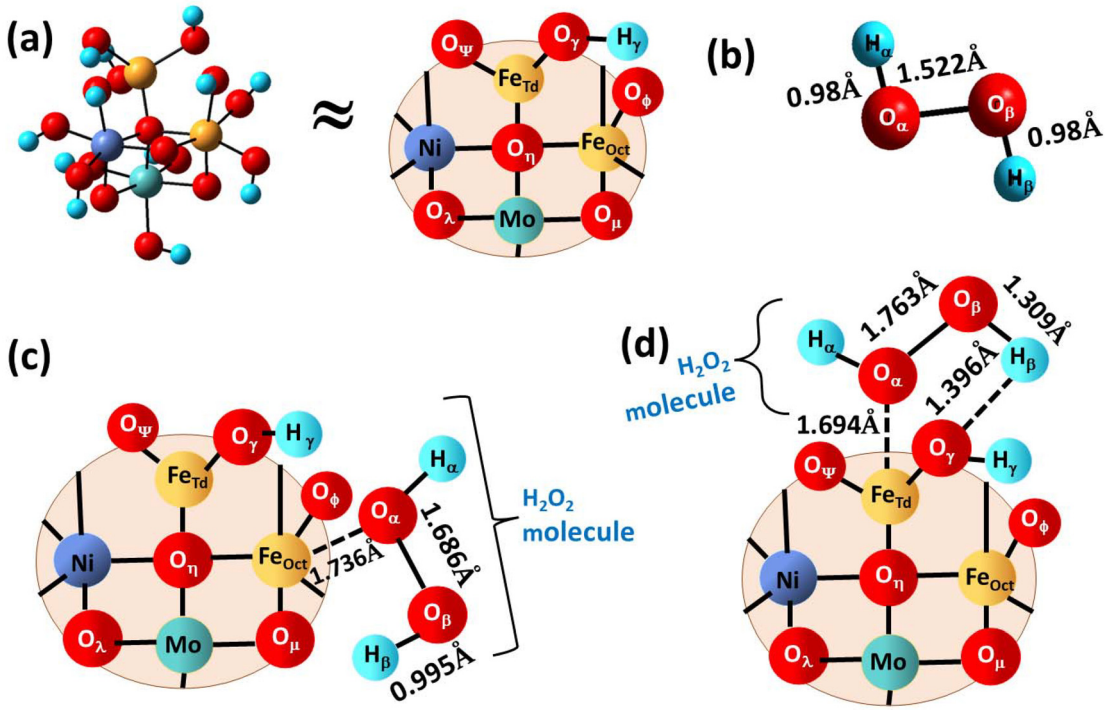

Fig. 11 (a) A 2-dimensional projection of the MoNIF model showing the abbreviations used for various atom types. (b) The optimized model of H_2O_2 molecule showing various bond lengths; (c) displays various interaction lengths in H_2O_2_Fe(Oct)_MoNIF_GS, and (d) depicts various interaction lengths in the H_2O_2_Fe(Td)_MoNIF_ES systems.

Table 2 The delocalization energy ($E^{(2)}$ in kcal mol^{-1}) analysis of charge transfer from donor to acceptor NBO of the H_2O_2_Fe(Oct)_MoNIF_GS, and H_2O_2_Fe(Td)_MoNIF_ES systems. "LP" indicates the 1-center nonbonding lone pair electrons, "LP*" signifies a 1-center vacant orbital, "BD" abbreviates 2-center bonding (σ) orbital, and "BD*" represents a 2-center antibonding σ* orbital

System	Donor NBO	Acceptor NBO	$E^{(2)}$ (kcal mol^{-1})
H_2O_2_Fe(Oct)_MoNIF_GS	LP(Fe_{Oct})	BD*(O_α–O_β)	0.52
	BD(O_α–O_β)	LP*(Fe_{Oct})	4.51
	BD(Fe_{Oct}–O_μ)	LP*(Mo)	24.67
	LP(Mo)	BD*(Fe_{Oct}–O_μ)	3.08
H_2O_2_Fe(Td)_MoNIF_ES	LP(Fe_{Td})	BD*(O_α–O_β)	17.38
	BD(O_α–O_β)	LP*(Fe_{Td})	16.31
	BD(Mo–O_η)	LP*(Fe_{Td})	20.79
	LP(O_γ)	BD*(H_β–O_β)	7.57

slight activation of O_α–O_β bond of H_2O_2 molecule. In contrast, the BD (Fe_{Oct}–O_μ) charge transfer to the LP*(Mo) occurs with a considerably higher $E^{(2)}$ value *i.e.* 24.67 kcal mol^{-1}. On the contrary, the charge transfer from LP(Mo) to BD*(Fe_{Oct}–O_μ) only has 3.08 kcal mol^{-1} $E^{(2)}$ value.

In H_2O_2_Fe(Td)_MoNIF_ES system, charge transfer takes place from LP (Fe_{Td}) to BD*(O_α–O_β) with 17.38 kcal mol^{-1} delocalization energy. Concurrently, a back donation occurs from BD(O_α–O_β) to LP*(Fe_{Td}) with 16.31 kcal mol^{-1} $E^{(2)}$ value. Both charge transfers are the reasons for the significantly increased weakening and activation of the O_α–O_β bond of H_2O_2 molecule in the photoexcited state. On the other hand, charge transfer occurs from BD(Mo–O_η) to LP*(Fe_{Td}) with 20.79 kcal mol^{-1} $E^{(2)}$ value. This charge transfer promotes the earlier two charge transfers between $Fe^{(2)}$ and O_α–O_β related NBOs. Complementary to this, another charge transfer takes place from LP (O_γ) to BD*(H_β–O_β) with 7.57 kcal mol^{-1} interaction energy. Hence, the delocalization in the H_2O_2_Fe(Td)_MoNIF_ES system is considerably larger. Consequently, the bond activation of O_α–O_β bond of H_2O_2 molecule is more in photoexcited state than in ground state, which leads to the efficient formation of OH$^\bullet$ radicals during the photocatalytic reaction.

3.4. Photo-Fenton degradation mechanism

Fig. 12 illustrates the proposed mechanism for the photo-Fenton degradation of TC by the Mo-doped $NiFe_2O_4$ photocatalyst. Experimental results from UV-DRS and Mott–Schottky

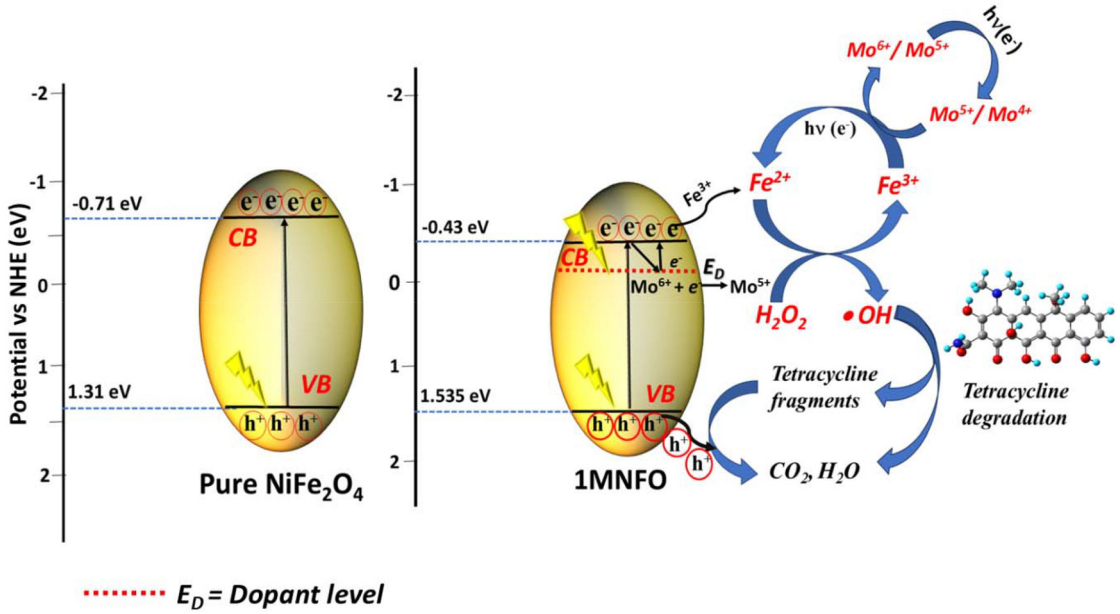

Fig. 12 Plausible mechanism for photo-Fenton degradation of TC by 1MNFO photocatalyst.

analysis revealed that Mo doping reduced the band gap and shifted the VB and CB band edges to higher (or more positive) values. Among all the doped samples, the 1% Mo-doped $NiFe_2O_4$ exhibited the best photo-Fenton activity, attributed to its lowest charge transfer resistance and highest charge separation efficiency, as confirmed by the Nyquist plot. The 1MNFO sample exhibits negligible dark Fenton degradation of TC. Contrary to this, the 1MNFO particles show high visible light photo-Fenton TC degradation activity.

DFT studies reveal that HOMO in the MoNIF (a cluster model of 1MNFO) system shifts from Fe(Oct) in the ground state to Fe(Td) in the photoexcited state. TDDFT calculations indicate that the excited state HOMO is localized on the Fe(Td) center. Effectively, the Fe^{3+} occupying the Td site in 1MNFO is reduced to Fe^{2+} by the photoexcited electrons. H_2O_2 interacts more effectively with the photoexcited model through the Fe (Td) site causing greater activation of its O–O bond and $OH^{\bullet}$ radical generation. Scavenger experiments confirm that $OH^{\bullet}$ radicals are the active species responsible for the photo-Fenton activity. These $OH^{\bullet}$ radicals and photogenerated holes subsequently react with tetracycline (TC), oxidizing it into smaller aliphatic fragments (eqn (14)–(16)).

Overall, suitable visible light irradiation photogenerates electron/hole pairs in the photocatalyst (eqn (9)). The photoexcited electrons can reduce Fe^{3+} to Fe^{2+} on the surface of the photocatalyst (eqn (10)). Because the redox potential of Mo^{6+}/Mo^{5+} is approximately 0.4 eV,[15,38] the Mo dopant energy level just below the CB of 1MNFO can trap photogenerated carriers, enhancing charge separation and prolonging the charge carrier lifetimes (eqn (11)). Once Mo^{6+} captures electrons, it is reduced to Mo^{5+}, forming a redox-active species capable of further reactions. Mo^{5+} then interacts with H_2O_2 and facilitates the decomposition of H_2O_2 into $^{\bullet}OH$. Through this reaction, Mo^{5+} is oxidized back to Mo^{6+}, ensuring the continuous regeneration of active sites and maintaining the catalytic cycle. The detection of Mo^{4+} in the Mo 3d XPS of recycled 1MNFO sample further implies a redox cycle involving Mo in +6, +5, and +4 oxidation states, potentially contributing to enhanced catalytic performance. The dopant level electrons can also get photoexcited to convert Fe^{3+} to Fe^{2+} in the 1MNFO photocatalyst (eqn (12)). The latter interacts and reduces H_2O_2 to generate $^{\bullet}OH$ radicals (eqn (13) and (14)).

$$1MNFO + h\nu \rightarrow 1MNFO(e_{cb}^{-} + h_{vb}^{+}) \quad (9)$$

$$Fe^{3+} + e_{cb}^{-} \rightarrow Fe^{2+} \quad (10)$$

$$Mo^{6+}/Mo^{5+} + e_{cb}^{-} \rightarrow Mo^{5+}/Mo^{4+} \quad (11)$$

$$Mo^{5+}/Mo^{4+} + Fe^{3+} \rightarrow Fe^{2+} + Mo^{6+}/Mo^{5+} \quad (12)$$

$$e^{-} + H_2O_2 \rightarrow {}^{\bullet}OH + OH^{-} \quad (13)$$

$$Fe^{2+} + H_2O_2 \rightarrow Fe^{3+} + {}^{\bullet}OH + OH^{-} \quad (14)$$

$$^{\bullet}OH + \text{tetracycline} \rightarrow \text{TC fragments}/CO_2 + H_2O \quad (15)$$

$$h^{+} + \text{TC fragments} \rightarrow CO_2 + H_2O \quad (16)$$

4. Conclusions

The spinel superparamagnetic $NiFe_2O_4$ semiconductor is a potential candidate for photo-Fenton degradation of organic pollutants due to its visible light band gap, photochemical stability, and magnetic separability. However, it suffers from

low surface reaction rates, rapid electron–hole recombination, and poor visible light absorption. Mo doping addresses these limitations by enhancing charge separation and reducing charge recombination through the introduction of dopant levels in the band structures. Mo-doped $NiFe_2O_4$ photocatalysts were synthesized by a one-step hydrothermal method. A comparison of the Nyquist plots of the investigated samples shows that the 1% Mo-doped $NiFe_2O_4$ sample has the best charge transfer kinetics. The 1% Mo-doped $NiFe_2O_4$ demonstrated excellent photo-Fenton degradation of tetracycline, with appropriate recyclability. The TOF value of 1% Mo-doped $NiFe_2O_4$ photocatalyst is higher than other doped semiconductor photocatalysts previously reported.

Mo-doped $NiFe_2O_4$ has a reduced band gap (and the shifting of its band edges) show that the dopant Mo acts both as an electron trapper and supplier, improving charge separation and carrier lifetimes during the photo-Fenton process. DFT and TDDFT studies reveal that in the Mo-doped $NiFe_2O_4$ (MoNIF) system, the HOMO shifts from Fe(Oct) in the ground state to Fe(Td) in the excited state. Additionally, Fe(Td) of Mo doped $NiFe_2O_4$ activates the O–O bond of H_2O_2 more effectively in the excited state, producing hydroxyl radicals. DFT and experimental results enable us to propose an effective mechanism for photo-Fenton TC degradation.

Data availability

Data are available upon request from the authors.

Conflicts of interest

There are no conflicts to declare.

Acknowledgements

The author (Anshu Shrivastava) acknowledges to CSIR-UGC for granting senior research fellowship (ref. no. 379/(CSIR UGC NET JUNE2019)). We express thanks to Prof. Anup Kumar Ghosh (Department of Physics, BHU) for providing VSM facility. The authors further acknowledge CIF-IITBHU for offering several facilities for material characterisation. The computational resources provided by the centre for computing and information service (CCIS) at IIT(BHU) are acknowledged.

References

1 B. L. Phoon, C. C. Ong, M. S. Mohamed Saheed, P. L. Show, J. S. Chang, T. C. Ling, S. S. Lam and J. C. Juan, *J. Hazard. Mater.*, 2020, **400**, 122961.
2 F. Ahmad, D. Zhu and J. Sun, *Environ. Sci.*, 2021, **33**(1), 64.
3 A. Kumari, N. S. Maurya and B. Tiwari, *Curr. Dev. Biotechnol. Bioeng.*, 2020, 549–570.
4 S. Li, Y. Wu, H. Zheng, H. Li, Y. Zheng, J. Nan, J. Ma, D. Nagarajan and J. S. Chang, *Chemosphere*, 2023, **311**, 136977.
5 M. Muruganandham, R. P. S. Suri, S. Jafari, M. Sillanpää, G. J. Lee, J. J. Wu and M. Swaminathan, *Int. J. Photoenergy*, 2014, **2014**, 821674.
6 A. Mirzaei, Z. Chen, F. Haghighat and L. Yerushalmi, *Chemosphere*, 2017, **174**, 665–688.
7 A. Deb, J. Rumky and M. Sillanpää, in *Advanced Oxidation Processes for Micropollutant Remediation*, CRC Press, 2023, pp. 157–185.
8 M. A. Hassaan, M. A. El-Nemr, M. R. Elkatory, S. Ragab, V. C. Niculescu and A. El Nemr, *Top. Curr. Chem.*, 2023, **381**, 1–54.
9 A. Ren, C. Liu, Y. Hong, W. Shi, S. Lin and P. Li, *Chem. Eng. J.*, 2014, **258**, 301–308.
10 X. Li, H. Xu, L. Wang, L. Zhang, X. F. Cao and Y. C. Guo, *J. Taiwan Inst. Chem. Eng.*, 2018, **85**, 257–264.
11 F. M. A. Alzahrani, A. Irshad, S. Zulfiqar, Z. A. Alrowaili, N. ul Ain, A. Anwar, M. Farooq Warsi and M. S. Al-Buriahi, *J. Rare Earths*, 2023, **41**, 1919–1928.
12 F. M. Fatimah, S. T. Almutairi, A. Anwar, A. Irshad, Z. A. Alrowaili, H. Sabeeh, S. Zulfiqar and M. S. Al-Buriahi, *Mater. Sci. Eng., B*, 2023, **297**, 116794.
13 S. Kanithan, N. Arun Vignesh, K. M. Katubi, P. S. Subudhi, E. Yanmaz, J. Arockia Dhanraj, N. S. Alsaiari, K. M. Abualnaja, M. Sukumar, M. Sundararajan, S. Baskar, S. Sahu and C. S. Dash, *J. Mol. Struct.*, 2022, 1265.
14 R. Mohammadzadeh Kakhki, A. Khorrampoor, M. Rabbani and F. Ahsani, *J. Mater. Sci.: Mater. Electron.*, 2017, **28**, 4095–4101.
15 Y. Yang, X. J. Li, J. T. Chen and L. Y. Wang, *J. Photochem. Photobiol., A*, 2004, **163**, 517–522.
16 M. Yadav, U. Kumar, A. Kumar De and I. Sinha, *Phys. Chem. Chem. Phys.*, 2024, **26**, 22442–22453.
17 J. Kuntail, U. Kumar and I. Sinha, *Mol. Catal.*, 2022, **528**, 112491.
18 J. Kuntail, S. Pal and I. Sinha, *J. Mol. Liq.*, 2020, 318.
19 A. Shrivastava, U. Kumar and I. Sinha, *Ind. Eng. Chem. Res.*, 2024, **63**, 15721–15734.
20 J. P. Perdew, K. Burke and M. Ernzerhof, *Phys. Rev. Lett.*, 1996, **77**, 3865.
21 A. Jain, S. P. Ong, G. Hautier, W. Chen, W. D. Richards, S. Dacek, S. Cholia, D. Gunter, D. Skinner, G. Ceder and K. A. Persson, *APL Mater.*, 2013, **1**, 11002.
22 MAPS Platform – SCIENOMICS, **https://www.scienomics.com/maps-platform/**, (accessed 31 March 2023).
23 C. Sosa, J. Andzelm, B. C. Elkin, E. Wimmer, K. D. Dobbs and D. A. Dixon, *J. Phys. Chem.*, 1992, **96**, 6630–6636.
24 A. Shrivastava, J. Kuntail, U. Kumar and I. Sinha, *J. Mol. Liq.*, 2023, 389.
25 R. D. Shannon, *Acta Crystallogr., Sect. A*, 1976, **32**, 751–767.
26 P. Priyadharshini and K. Pushpanathan, *Chem. Phys. Impact*, 2023, 6.
27 T. Yamashita and P. Hayes, *Appl. Surf. Sci.*, 2008, **254**, 2441–2449.

28 M. Muhler, R. Schlogl and A. G. Ertl, *J. Catal.*, 1992, **138**, 416–444.
29 D. D. Hawn and B. M. Dekoven, *Surf. Interface Anal.*, 1987, **10**, 63–74.
30 P. Mills and J. L. Sullivan, *J. Phys. D: Appl. Phys.*, 1983, **16**, 723.
31 N. Wang, R. X. Wang, Z. J. Li, R. Liu, H. Gao, H. Y. Chen, R. Li, Y. Z. Long and H. Di Zhang, *ACS Appl. Nano Mater.*, 2023, **6**, 15063–15072.
32 S. Chen, H. Liao, X. Xu, R. Wang, Z. Sun and L. Huang, *Inorg. Chem. Front.*, 2023, **10**, 6320–6328.
33 J. C. C. Fan and J. B. Goodenough, *J. Appl. Phys.*, 1977, **48**, 3524–3531.
34 N. Sarin, M. Mishra, G. Gupta, M. Arora and V. Luthra, *Phys. Status Solidi B*, 2018, **255**, 1700683.
35 A. Klasen, P. Baumli, Q. Sheng, E. Johannes, S. A. Bretschneider, I. M. Hermes, V. W. Bergmann, C. Gort, A. Axt, S. A. L. Weber, H. Kim, H. J. Butt, W. Tremel and R. Berger, *J. Phys. Chem. C*, 2019, **123**, 13458–13466.
36 J. Choi and L. Thompson, XPS study of as-prepared and reduced molybdenum oxides, *Appl. Surf. Sci.*, 1996, **93**, 143–149.
37 V. Kumaravel, S. Rhatigan, S. Mathew, M. C. Michel, J. Bartlett, M. Nolan, S. J. Hinder, A. Gascó, C. Ruiz-Palomar, D. Hermosilla and S. C. Pillai, *J. Phys. Mater.*, 2020, 3.
38 Y. Jiang, W. F. Chen, P. Koshy and C. C. Sorrell, *J. Mater. Sci.*, 2019, **54**, 5266–5279.
39 S. Esposito, N. Ditaranto, G. Dell'Agli, R. Nasi, P. Rivolo and B. Bonelli, *ACS Omega*, 2021, **6**, 5379–5388.
40 Y. H. Ahmad, A. S. Abu Hatab, A. T. Mohamed, M. S. Al-Kuwari, A. S. Aljaber and S. Y. Al-Qaradawi, *Nanomaterials*, 2022, **12**, 2051.
41 N. Jatav, A. Shrivastava, A. Kumar De and I. Sinha, *J. Environ. Chem. Eng.*, 2022, **10**, 107975.
42 C. E. Tan, E. C. Su and M. Y. Wey, *Appl. Surf. Sci.*, 2022, **590**, 152954.
43 J. Liu, Z. Liu, C. Piao, S. Li, J. Tang, D. Fang, Z. Zhang and J. Wang, *J. Power Sources*, 2020, **469**, 228430.
44 S. S. Shinde, C. H. Bhosale, K. Y. Rajpure and J. H. Lee, *J. Photochem. Photobiol., B*, 2014, **141**, 210–216.
45 X. Zheng, J. Yuan, J. Shen, J. Liang, J. Che, B. Tang, G. He and H. Chen, *J. Mater. Sci.: Mater. Electron.*, 2019, **30**, 5986–5994.
46 Z. Luo, M. Y. Tseng, D. Minakata, L. Bai, W. P. Hu, W. Song, Z. Wei, R. Spinney, D. D. Dionysiou and R. Xiao, *Chem. Eng. J.*, 2021, **410**, 128181.
47 S. Singh, A. Shrivastava, D. K. Singh, M. Yadav, V. Singh, V. Rathour, A. Tiwari, I. Sinha and V. Ganesan, *Int. J. Hydrogen Energy*, 2024, **56**, 188–198.